Engineering Analysis with Boundary Elements 169 (2024) 105953

Contents lists available at ScienceDirect

Engineering Analysis with Boundary Elements

journal homepage: www.elsevier.com/locate/enganabound

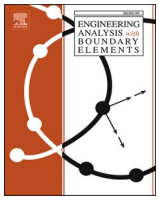

# Phase-field formulated meshless simulation of axisymmetric Rayleigh-Taylor instability problem

K.B. Rana [a], B. Mavrič [a,b], R. Zahoor [a], B. Šarler [a,b,*]

[a] Faculty of Mechanical Engineering, University of Ljubljana, Aškerčeva cesta 6 1000 Ljubljana, Slovenia
[b] Institute of Metals and Technology, Lepi pot 11 1000 Ljubljana, Slovenia

ARTICLE INFO

*Keywords:*
Two-phase flow
Phase-field
Two-dimensional
Axisymmetric
Diffuse approximate method
PISO

ABSTRACT

A formulation of the immiscible Newtonian two-liquid system with different densities and influenced by gravity is based on the Phase-Field Method (PFM) approach. The solution of the related governing coupled Navier-Stokes (NS) and Cahn-Hillard (CH) equations is structured by the meshless Diffuse Approximate Method (DAM) and Pressure Implicit with Splitting of Operators (PISO). The variable density is involved in all the terms. The related moving boundary problem is handled through single-domain, irregular, fixed node arrangement in Cartesian and axisymmetric coordinates. The meshless DAM uses weighted least squares approximation on overlapping sub-domains, polynomial shape functions of second-order and Gaussian weights. This solution procedure has improved stability compared to Chorin's pressure-velocity coupling, previously used in meshless solutions of related problems. The Rayleigh-Taylor instability problem simulations are performed for an Atwood number of 0.76. The DAM parameters (shape parameter of the Gaussian weight function and number of nodes in a local subdomain) are the same as in the authors' previous studies on single-phase flows. The simulations did not need any upwinding in the range of the simulations. The results compare well with the mesh-based finite volume method studies performed with the open-source code Gerris, Open-source Field Operation and Manipulation (OpenFOAM®) code and previously existing results.

## 1. Introduction

Rayleigh-Taylor (RT) instability is a hydrodynamic instability which is easiest to observe when we invert a glass full of water. When the glass is inverted, the less dense air cannot support the water, and instability begins to grow between the denser fluid (water) and the less dense fluid (air), ending with water falling out of the glass. The theoretical foundation of RT instability was laid by Lord Rayleigh in 1883 [1] and further developed by G. I. Taylor for accelerated fluids in 1950 [2]. The phenomenon describes the entrance of the heavier fluid as mushroom-shaped protrusions into a lighter fluid. The first experiment to validate this theory was performed in 1950 by G. Lewis [3]. The analytical studies to cope with the RT instability phenomenon mainly considered small density ratios or a negligible density of the lighter fluids [4,5]. The difficulties in the analytical studies carved a path for the numerical models, the earliest of which was presented in [6]. However, models based on the marker-and-cell method [7,8] were the first to succeed. The study [9] comprehensively reviews the existing experimental, analytical and numerical literature about the RT instability phenomenon. Most numerical simulations of the RT instability [5,10–12] involve the Boussinesq approximation [13]. This approximation is handy for buoyancy-driven flows with small density variations. It assumes that the density variations do not affect the inertial forces acting on the fluid. Therefore, density is treated as a constant everywhere in the momentum equation except for the terms that involve gravity, i.e., the buoyancy term. The present model deals with the large density ratio and high Atwood number and does not involve the Boussinesq approximation, i.e., the density variation is included in all the terms. This generalisation makes the numerical model applicable to a much wider range of moving-boundary, two-phase, immiscible flow problems.

To accurately model a two-phase moving boundary flow, proper handling of the interface between the phases, the discontinuities in the material properties across the interface, and proper implementation of the interfacial boundary conditions are crucial. The commonly used numerical methods for simulating two-phase flows are categorised as sharp interface and diffuse interface methods. Sharp interface methods treat the interface or moving boundary between two phases as an

* Corresponidng author.
*E-mail address:* bozidar.sarler@fs.uni-lj.si (B. Šarler).

https://doi.org/10.1016/j.enganabound.2024.105953
Received 29 March 2024; Received in revised form 5 September 2024; Accepted 7 September 2024
Available online 14 September 2024

infinitely thin, sharp layer. A moving mesh handles the moving interface, and the material properties change sharply across the interface. The nodes are placed on the interface, and the mesh is deformed according to the flow on both sides. Some of the most famous studies using the moving mesh are [14–21]. Sharp interface methods have been used to study the dynamics of viscous drops in a co-flow capillary tube [22], the growth and detachment of a gas bubble in a non-rotational flow [23] and stable, accurate and robust computation of incompressible, immiscible fluids for bubble and liquid jet formation [24] and several others [25,26]. Moving mesh comes with the increased computational cost of re-meshing and the related introduction of interpolation error. Furthermore, mesh entanglement occurs due to the large displacement of the initial domain shape, which limits the sharp interface formulation to relatively mild changes of the topology.

As an alternative, fixed-grid methods such as Volume of Fluid (VOF) [27], Level Set Method (LSM) [28] and Phase Field Method (PFM) [29] were successful in treating deformed interfaces. Both LSM and VOF are the most powerful and versatile numerical tools for tracking the evaluation of the interface and have been used for a wide range of two-phase flow problems. The VOF method is the most common and oldest fixed-grid method that has been used to investigate the droplet formation in an axisymmetric co-flow microchannel [27], to analyse the impact of a Newtonian drop on a thin circular fibre [30] and an FVM-based numerical modelling of the Gas Dynamic Virtual Nozzles (GDVNs) to generate liquid microjets [31,32]. The VOF method roughly estimates the moving interface and its curvature. Further, the interface reconstruction from the discontinuous fraction function at each time step is computationally demanding. The main drawback of the LSM is the smearing of the interface and the difficulty of ensuring mass conservation.

On the contrary, the PFM for multiphase flows is easier to implement and inherently conservative for two-phase flows. It assumes that the interface is diffused physically rather than in a numerical sense. The interface is described as a finite volumetric zone across which the physical properties vary steeply and continuously. The shape of the interface is determined by minimising the free energy of the interface. No explicit interface boundary condition is required at the moving boundary. The surface tension appears as a surface free energy per unit area caused by the gradient of the Phase Field (PF) variable.

In the literature, many applications of the PFM to the two- or multiphase flows are present, such as to simulate the three-phase flow [33] and to simulate the PF-formulated mixture of two incompressible fluids using a semi-discrete Fourier spectral method [34]. A detailed review of the development of PFM can be found in [35]. PFM has been developed for compressible binary mixtures based on the balance of mass, momentum, and energy by considering the second law of thermodynamics. It has been proved analytically and numerically that the developed model can describe the phase equilibrium for a binary mixture of $CO_2$ and ethanol by changing the parameters, which measure the attraction force between molecules of both components [36]. The study [37] presented a continuum formulation of the immiscible flow hydrodynamics based on Navier-Stokes equations and Cahn-Hilliard interfacial energy, and it was shown that the PFM simulations are in close agreement with the molecular dynamics reference simulations. A one-fluid multicomponent numerical formulation was adopted to systematically derive the thermodynamically consistent hydrodynamic PFM for compressible viscous fluid mixtures [38]. PFM was used to demonstrate the drop formation process and the effect of various physical parameters on the dynamics of the droplet when a Newtonian fluid is injected into another co-flowing immiscible, Newtonian fluid with different viscosity and density. The simulations were performed using a numerical method that involves a convex splitting scheme and a projection-type scheme for solving the Cahn Hilliard and momentum equations, respectively [39].

The present paper solves the classical RT instability benchmark test case with a meshless method. Meshless methods do not need any mesh to solve the partial differential equations rather the computational domain is discretized with irregularly distributed points without any pre-defined mesh connectivity between them. The classical mesh-based numerical methods such as the Finite Difference Method (FDM) [40], Finite Element Method (FEM) [41], Finite Volume Method (FVM) [42] and Boundary Domain Integral Method (BDIM) [43] are used in physical modelling of different engineering problems. These methods are very well established and offer powerful features. Still, they also involve inconveniences such as mesh generation and re-meshing, which are complex in moving boundary problems. Many meshless numerical methods [44–50] have evolved to overcome these limitations. Meshless methods are computationally very suitable for the problems where the nodes are added or removed during a simulation. Additionally, the meshless methods offer (i) flexibility in discretizing the problem geometry, (ii) simpler h-adaptivity, (iii) higher order continuous shape functions (iv) reduced node alignment sensitivity and (v) similar formulation in 2D and 3D problems. The authors employed strong-form meshless DAM in the advancements of the present paper because of its proven robustness in the regular and irregular node arrangements [46,51], easier implementation of higher-order polynomial shape function and successful implementation in the preliminary studies [52–54].

DAM was initially proposed in [50] and was later used in studies [55–57]. The studies [58–61] popularised DAM for heat transfer and fluid flow problems. One of the first industrial applications of DAM is presented in [62]. A few successful implementations of DAM in solid mechanics include [51,63–65]. The recent studies about the drop-formation at the nozzle orifice due to the effect of co-flowing incompressible gas [66] and simulation of RT instability with Boussinesq approximation [11] proved that the combination of DAM and PFM is a valuable numerical tool for solving immiscible, convective hydrodynamic problems. Therefore, the authors used the same combination for a two-phase flow solver in the present work. The simulations were first run in a two-dimensional (2D) Cartesian coordinate system between two vertical parallel plates, and the results were compared with the reference FVM simulations performed using open-source code Gerris [67,68] and in the previous Boussinesq-based study [11]. Afterwards, the simulations in the present paper were performed in a cylinder using axisymmetric coordinate system. The verification was made by comparing our meshless results with the FVM simulations performed by Open-source Field Operation and Manipulation (OpenFOAM®) [69] code. Compared to the previous meshless simulations of related numerical examples [11], the present model uses non-Boussinesq approximation, irregular node arrangement and improved stability by employing Pressure Implicit with Splitting of Operators (PISO) [70] pressure velocity coupling algorithm instead of Chorin's pressure velocity coupling [71]. The tested DAM parameters such as shape parameter of the Gaussian weight function $a_0$ and the number of nodes in a local subdomain $n_{loc}$ are the same as in the authors' preliminary studies of single-phase flow [52–54].

## 2. Physical model

### 2.1. Governing equations

The two-phase, viscous, incompressible, immiscible fluid system is governed by the following coupled set of Navier-Stokes and Cahn-Hilliard equations

$$\frac{\partial \rho}{\partial t} + \nabla\cdot(\rho \mathbf{v}) = 0, \tag{1}$$

$$\frac{\partial (\rho \mathbf{v})}{\partial t} + \nabla\cdot(\rho \mathbf{v}\mathbf{v}) = -\nabla P + \mu\nabla^2\mathbf{v} + \mathbf{F}_{\mathrm{st}} + \mathbf{F}_{\mathrm{b}}, \tag{2}$$

$$\frac{\partial \varphi}{\partial t} + \mathbf{v}\cdot\nabla\varphi = E\nabla^2\psi, \tag{3}$$

**Table 1**
Material properties of the fluid and PF parameters used in the simulations.

| Material property/parameter | symbol | value |
|---|---|---|
| Density of the heavier fluid | $\rho_1$ | 1.225 kg /m$^3$ |
| Density of the lighter fluid | $\rho_2$ | 0.1694 kg /m$^3$ |
| Viscosity of both fluids | $\mu_1 = \mu_2$ | 0.00313 kg /(ms) |
| Surface tension | $\sigma$ | 1.0 N /m |
| Mobility | $E$ | $9.0 \times 10^{-4}$ m$^4$ /(N s) |
| Interface width | $\xi$ | 0.01m |
| Magnitude of free energy | $\lambda$ | 0.011N |

$$\psi = \frac{\lambda}{\xi^2}(\varphi^3 - \varphi) - \lambda\nabla^2\varphi \tag{4}$$

where $\rho$, $\mathbf{v}$, $P$, $\mu$ and $t$ stand for effective density, velocity, pressure, effective dynamic viscosity and time, respectively. $\mathbf{F}_{st} = -\lambda\left(\nabla^2\varphi\nabla\varphi + \frac{1}{2}\nabla(\nabla\varphi\cdot\nabla\varphi)\right)$ represents the surface tension force and $\mathbf{F}_b = \rho\mathbf{g}$ represents the body force, while $\varphi$, $\lambda$,$E$,$\psi$, $\xi$, $\sigma$ and $\mathbf{g}$ denote the PF variable, magnitude of free energy, mobility, chemical potential, interface thickness, surface tension and gravitational acceleration, respectively. The magnitude of free energy depends on surface tension

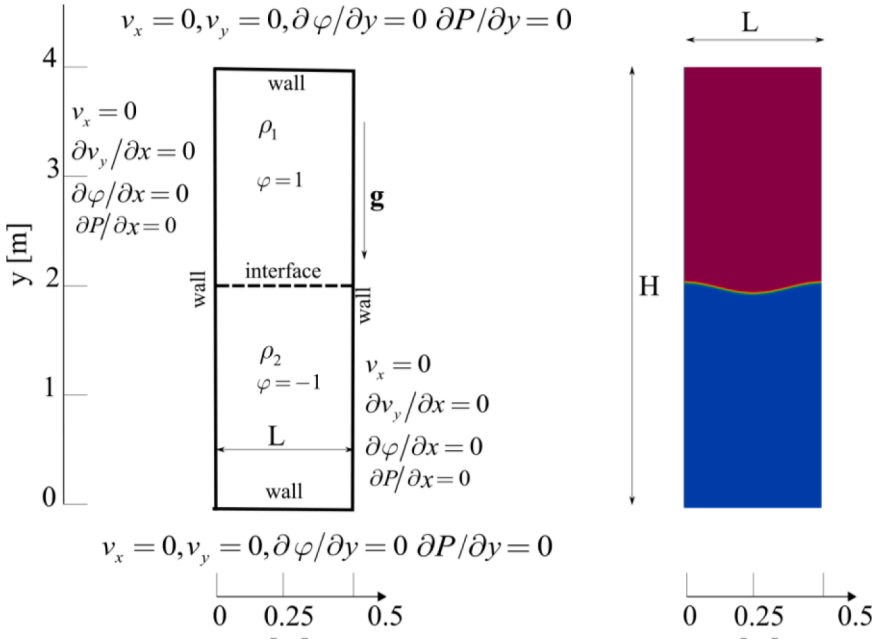


**Fig. 1.** Scheme of geometry and the boundary conditions of the two-dimensional Rayleigh-Taylor instability problem (left), Initial PF variable distribution at $t = 0$s in the cavity with $A = 0.05$m(right) obtained by Eq. (6).

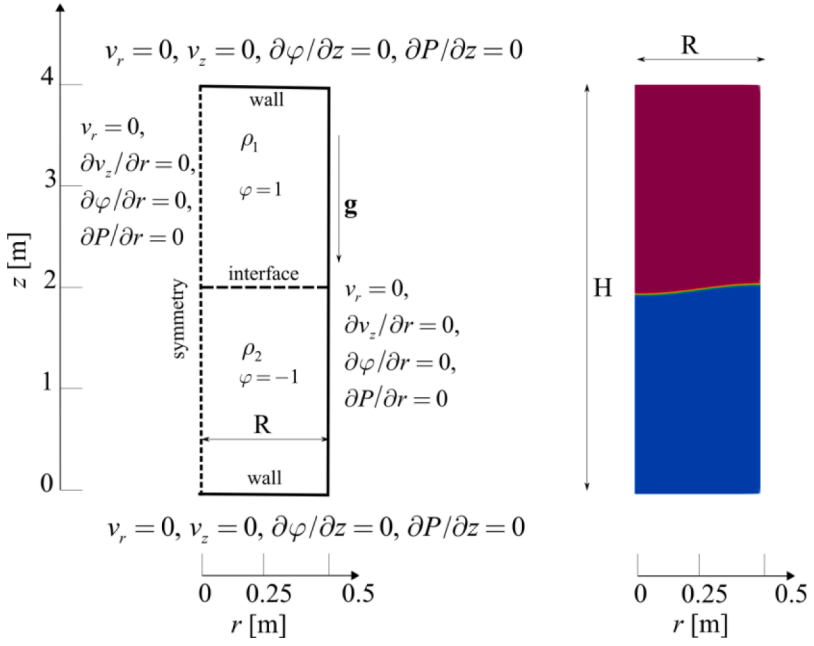


**Fig. 2.** Scheme of geometry and the boundary conditions of the axisymmetric Rayleigh-Taylor instability problem (left), Initial PF variable distribution at $t = 0$s in the cavity with $A = 0.05$m(right) obtained by Eq. (7).

**Table 2**
Nominal dimensions of the cavities.

| Geometry | Height ($H$) [m] | Width ($L$) [m] | Radius ($R$) [m] | symmetry axis |
|---|---|---|---|---|
| 2D cavity | 4.0 | 1.0 | – | – |
| AX cavity | 4.0 | – | 0.5 | at $r = 0$ m |

and interface thickness as $\lambda = \frac{3\alpha\xi}{2\sqrt{2}}$. The values of material properties of both fluids and PF parameters are shown in Table 1.

$\varphi = 1$ represents the top fluid with density $\rho_1$ and viscosity $\mu_1$ while $\varphi = -1$ represents the bottom fluid possessing density $\rho_2$ and viscosity $\mu_2$. In the present system $\rho_1 > \rho_2$ and $\mu_1 = \mu_2$ and Atwood number $At = \frac{\rho_1 - \rho_2}{\rho_1 + \rho_2}$ is kept at 0.76. The effective density is a smooth function of PF variable as

$$\rho = \rho_1\left(\frac{1+\varphi}{2}\right) + \rho_2\left(\frac{1-\varphi}{2}\right). \tag{5}$$

### 2.2. Computational domain, boundary, and initial conditions

Consider solving the two-phase RT instability phenomenon using the governing Eqs. (1) to (4). A scheme of the RT instability problem in Cartesian and axisymmetric coordinate systems and their respective boundary conditions are provided in Fig. 1 and Fig. 2, respectively. Hereafter, in this paper, the 2D abbreviation refers to the problem presented in Fig. 1, while AX to the problem presented in Fig. 2. The nominal dimensions of both cavities are shown in Table 2. Each cavity is filled with two incompressible, immiscible fluids possessing different constant densities and the same constant viscosities stated in Table 1. The heavier fluid is placed above the lighter fluid.

The boundary conditions for each of the 2D and AX cavities are as follows: No-slip velocity boundary condition is applied at the top and bottom walls, while free-slip velocity boundary condition is applied on the side walls and the symmetry axis. Neumann boundary conditions for pressure and PF variables are enforced at all the walls and the symmetry axis. Initially at $t = 0$, the fluids are at rest, and the pressure is zero everywhere. For the PF variable, an initial profile perturbed by a sinusoidal wave of amplitude $A = 0.05$m is given by the function

$$\varphi = \tanh\left(y - 2 + A\cos(2\pi x) \Big/ \sqrt{2}\xi\right), \tag{6}$$

for the 2D cavity and by the function

$$\varphi = \tanh\left(z - 2 + A\cos(\pi r) \Big/ \sqrt{2}\xi\right) \tag{7}$$

for the AX cavity. The initial profiles of the PF variable are shown in Figs. 1 and 2.

## 3. Solution procedure

### 3.1. Diffuse approximate method (DAM)

The Weighted Least Squares (WLS) approach is used in DAM to determine a locally smooth and differentiable approximation of discrete data. The local shape functions are defined separately for each computational node and its associated subdomain, making the method local. The approximation of function is defined as the dot product of the polynomial basis vector $\mathbf{b}(\mathbf{p}, \mathbf{p}_l)$ and the vector of the approximation coefficients $\mathbf{c}_l$

$$\widehat{f}_l(\mathbf{p}) = \mathbf{b}(\mathbf{p}, \mathbf{p}_l)\cdot\mathbf{c}_l = \sum_{m=1}^{M} b_m(\mathbf{p}, \mathbf{p}_l)\, c_{l,m}, \tag{8}$$

where $\mathbf{p}_l$ is the position vector of the central node of the subdomain $l$, $\mathbf{p}$ is the position vector of any arbitrary point located inside that subdomain, and $M$ is the size of the polynomial basis vector. The concept of overlapping subdomains with boundary and domain nodes for an arbitrary-shaped computational domain is presented in Fig. 3. A node's local neighbourhood is created through k-d tree algorithm [72].

The bases consisting of second order polynomials are suitable for the present problem. For second order, the basis is

$$\mathbf{b}(\mathbf{p}, \mathbf{p}_l) = [1, (p_{ri} - p_{rl}), (p_{zi} - p_{zl}), (p_{ri} - p_{rl})(p_{zi} - p_{zl}), (p_{ri} - p_{rl})^2 (p_{zi} - p_{zl})^2]; M = 6, \tag{9}$$

Further, partial derivatives are applied to the approximation functions as

$$\mathscr{L}\widehat{f}_l(\mathbf{p}) = \mathscr{L}\,\mathbf{b}(\mathbf{p}, \mathbf{p}_l)\cdot\mathbf{c}_l, \tag{10}$$

where $\mathscr{L}$ is at most second-order linear differential operator. To obtain the vector of approximation coefficients $\mathbf{c}_l$ the following cost function $J_l$ is minimised by the WLS method

$$J_l = \sum_{i=1}^{n_{loc}} \theta(\mathbf{p}_i, \mathbf{p}_l)[f(\mathbf{p}_i) - \widehat{f}_l(\mathbf{p}_i)]^2, \tag{11}$$

where $f(\mathbf{p}_i)$ is the value at a point $\mathbf{p}_i$, $n_{loc}$ is the number of nodes in one local subdomain and $\theta$ is the Gaussian weight function. The minimisation of the cost function is performed by setting its partial derivative with respect to every unknown coefficient equal to zero

$$\frac{\partial J_l}{\partial c_{l,m}} = 0, \tag{12}$$

$$\sum_{i=1}^{n_{loc}} \theta(\mathbf{p}_i, \mathbf{p}_l) 2b_j(\mathbf{p}_i, \mathbf{p}_l)[\mathbf{b}(\mathbf{p}_i, \mathbf{p}_l)\cdot\mathbf{c}_l - f(\mathbf{p}_i)] = 0. \tag{13}$$

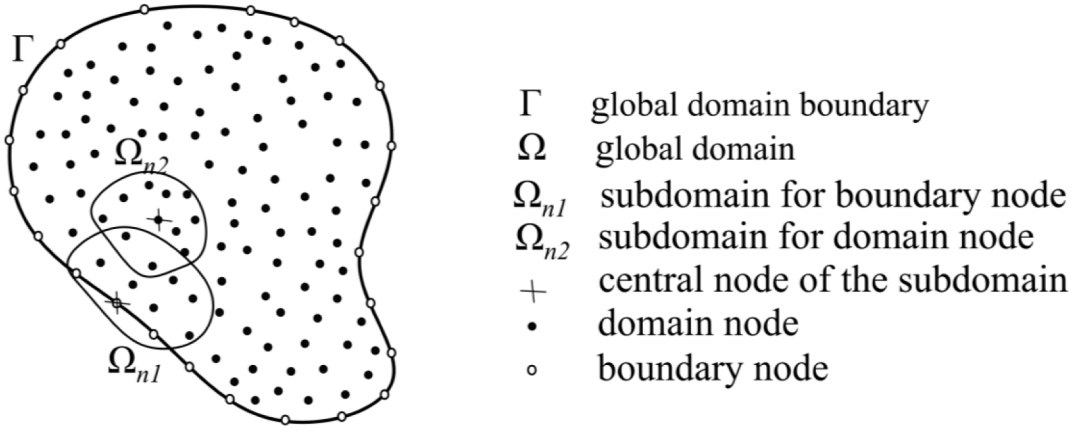


**Fig. 3.** Concept of overlapping subdomains.

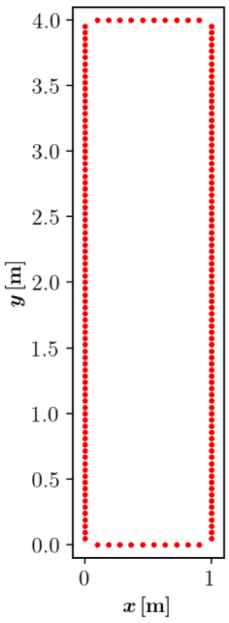


**Fig. 4.** Boundary nodes for uniform node arrangement.

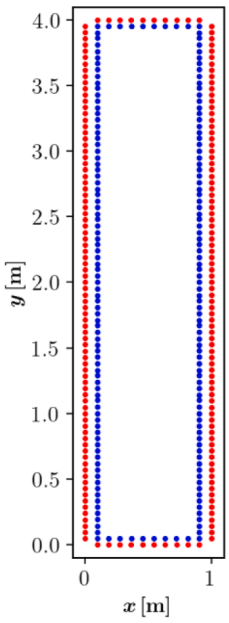


**Fig. 5.** Boundary (red) and inner boundary (blue) nodes for uniform node arrangement.

Dividing Eq. (13) by a constant and rearranging yields to a linear system of equations

$$\mathbf{A}_l \mathbf{c}_l = \mathbf{d}_l f(\mathbf{p}_i), \tag{14}$$

where $\mathbf{A}_l = \sum_{i=1}^{n_{loc}} \theta(\mathbf{p}_i, \mathbf{p}_l)\, \mathbf{b}(\mathbf{p}_i, \mathbf{p}_l)\mathbf{b}(\mathbf{p}_i, \mathbf{p}_l)$ and $\mathbf{d}_l = \sum_{i=1}^{n_{loc}} \theta(\mathbf{p}_i, \mathbf{p}_l)\, \mathbf{b}(\mathbf{p}_i, \mathbf{p}_l)$.

The Gaussian weight function is defined as

$$\theta(\mathbf{p}_i, \mathbf{p}_l) = \exp\left( - a_0 \frac{\| \mathbf{p}_i - \mathbf{p}_l \|^2}{h_l^2} \right), \tag{15}$$

where $a_0$ is the dimensionless shape parameter, which defines the width of the Gaussian weight and $h_l$is the distance between the central node of the subdomain and its farthest neighbour.

For local interpolation, Eq. (10) is written in summation as

$$\mathscr{L}\widehat{f}_l(\mathbf{p}) = \sum_k \mathscr{L}\mathbf{b}(\mathbf{p}, \mathbf{p}_l) \cdot \mathbf{c}_{l,k}. \tag{16}$$

For one node, the Eq. (14) changes to

$$\mathbf{c}_{l,k} = \sum_{j=1}^{n_{loc}} \mathbf{A}^{-1}_{l,k,j}\, \mathbf{d}_{l,j} f(\mathbf{p}_i). \tag{17}$$

All the right-sided terms of the Eq. (17) are constants except the field values $\widehat{f}_l(\mathbf{p})$ so

$$\widehat{f}_l(\mathbf{p}) = \sum_{i=1}^{n_{loc}} f(\mathbf{p}_i) w_i, \tag{18}$$

while all the discretization coefficients $w_i$ are determined before starting the subsequent solution steps.

### 3.2. Node spacing and arrangement

This subsection describes the procedure of node generation and space discretisation. The present work employs uniform and non-uniform node arrangements in the involved two geometrical arrangements. For example, the uniform and non-uniform node generation of 2D domain is presented here, but the process is similar in AX. The node generation procedure for uniform and non-uniform node arrangements is the same, except that the uniform node arrangement uses constant node density all over the domain. In contrast, the non-uniform node arrangement uses a position-dependent node density function, which gives a higher node density within the region of interest (0.5m $\leq H \leq$ 2.6m) than in the remaining domain. The region of interest for the 2D is 0.5m $\leq H \leq$ 2.6m and for the AX is 0.1m $\leq H \leq$ 2.6m.

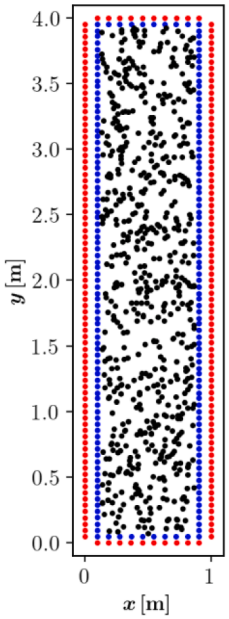


**Fig. 6.** Boundary (red), inner boundary (blue) and inner (black) nodes before the energy minimisation process for uniform node arrangement.

Firstly, the geometry is parametrised by a boundary function which considers the position-dependent node density function. The first node is positioned at the lower-left corner of the domain, followed by the positioning of subsequent boundary nodes counterclockwise according to the boundary shape. The positioning of boundary nodes for the uniform and non-uniform node arrangements is presented in Fig. 4 and Fig. 8, respectively. Then, the inner boundary nodes are placed as shown in Fig. 5 and Fig. 9. The inner boundary nodes are the immediate

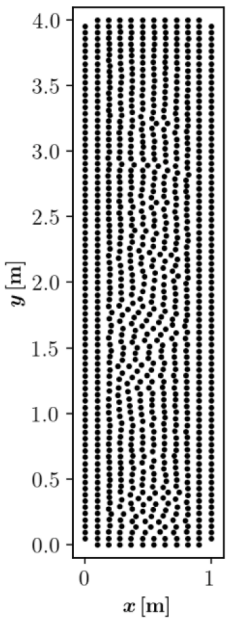


**Fig. 7.** Final node distribution after the energy minimisation process for uniform node arrangement. ($N = 1000$ generated by a constant density of 500 nodes per sq. m).

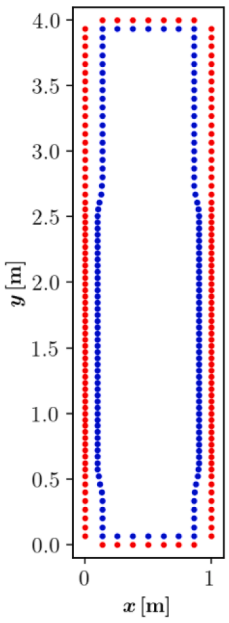


**Fig. 9.** Boundary (red) and inner boundary (blue) nodes for non-uniform node arrangement.

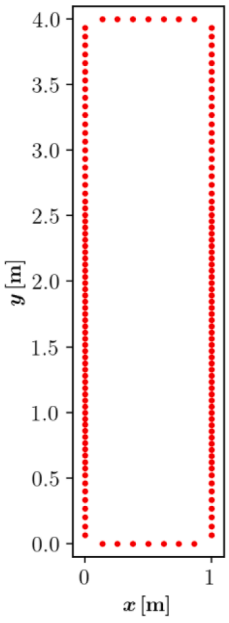


**Fig. 8.** Boundary nodes for non-uniform node arrangement.

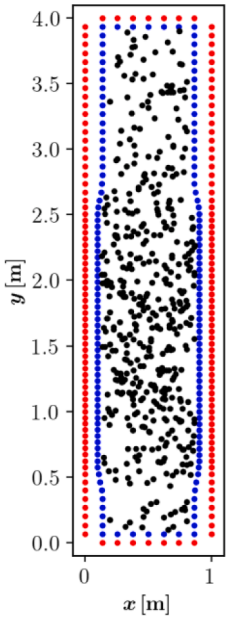


**Fig. 10.** Boundary (red), inner boundary (blue) and inner (black) nodes before the energy minimization process for non-uniform node arrangement.

neighbours of the boundary nodes. They are positioned in the opposite direction of the outward normal of the boundary nodes. The remaining inner nodes are randomly positioned inside the domain using the node density function and are presented in Fig. 6 and Fig. 10 for uniform and non-uniform node arrangements, respectively. A random position $\mathbf{p}_{\text{rnd}}$ is assigned to each node inside the domain. For each node, a random number $X_{\text{rnd}} \in [0, 1)$ and node density $\varsigma_{\mathbf{r}_{\text{rnd}}}$ are calculated. The position is accepted only if $X_{\text{rnd}} < \varsigma_{\mathbf{r}_{\text{rnd}}} / \varsigma_{\text{max}}$ where $\varsigma_{\text{max}}$ is the maximum node density value in the given geometry. It can be seen in Fig. 10 that the positions of the domain and boundary nodes are already adjusted according to the given node density function, i.e., denser nodes in the region of interest and coarser otherwise. Lastly, an energy minimisation procedure is performed for the randomly positioned inner nodes. Each point is allotted a charge that is inversely proportional to the prescribed local density, and the positions of the points are iteratively adjusted to minimise the "electrostatic" energy configuration.

The final configuration of uniform and non-uniform node arrangements is shown in Fig. 7 and Fig. 11, respectively. The node arrangements are generated at much lower node densities in graphical representation than in numerical simulations. The uniform node arrangement is generated by a user-defined node density $\chi_u = 500$. The node density function of the non-uniform node arrangement is given as

$$f_{den} = \chi_u[0.5 + (1 - 0.5)f_1 f_2], \tag{19}$$

and illustrated in Fig. 12. It combines two error functions $f_1 = (erf(-s_1 / w_0) + 1) / 2$ and $f_2 = (1 - erf(-s_2 / w_0)) / 2$ where $s_1 = 0.5$

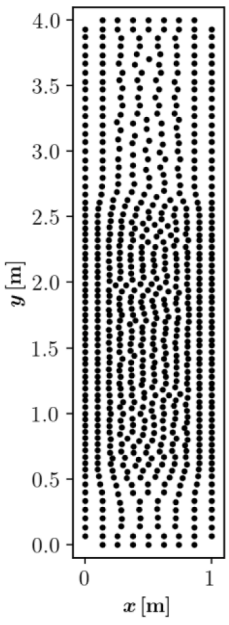


**Fig. 11.** Final node distribution after the energy minimization process for non-uniform node arrangement ($N = 763$ generated by node density function described in Eq. (19) and $\chi_u = 500$).

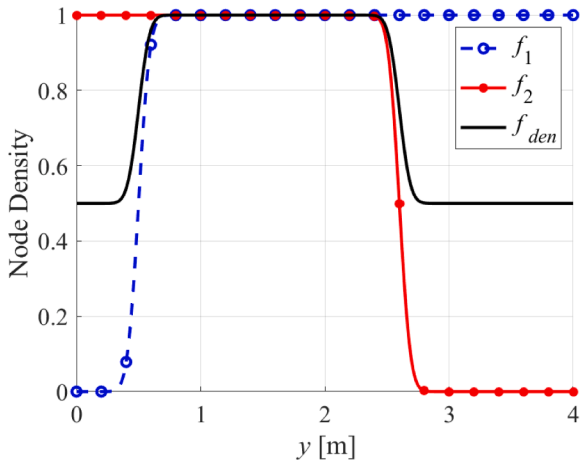


**Fig. 12.** Node density distribution function for non-uniform node arrangement. The final function $f_{den}$ is multiplied by a constant user-defined node density $\chi_u =$ 500 to create a node distribution with 763 nodes in the computational domain.

$- y$ and $s_2 = 2.6 - y$ are the distances of a node from the starting and ending point of the region of interest in $y$ direction.

### 3.3. Pressure implicit with splitting of operators

This study extends the classical PISO algorithm [70] for the pressure-velocity coupling of two-phase, incompressible flow. The key enhancement involves incorporating an additional corrector step that solves the Cahn-Hilliard equation, which governs the evolution of the PF variable. This incorporation ensures that the PF variable and the velocity field remain coupled within every time step. Hence, in one iteration, the two-phase PISO methodology performs one momentum predictor, two momentum correctors, and one PF variable corrector step. The unknown variables in PISO equations are marked red. Two-phase PISO methodology for incompressible flows works as follows:

**Momentum predictor step:** The momentum Eq. (2) is discretised implicitly and solved as

$$\left[\rho^n + \Delta t\left[\nabla\cdot(\rho^n\mathbf{v}^n) + (\rho^n\mathbf{v}^n)\cdot\nabla - \mu\nabla^2\right]\right]\mathbf{v}^* = \Delta t\left[-\lambda\left(\nabla^2\varphi^n\nabla\varphi^n + \frac{1}{2}\nabla(\nabla\varphi^n\cdot\nabla\varphi^n)\right) - \rho^n\mathbf{g} - \nabla P^n\right] + \rho^n\mathbf{v}^n, \tag{20}$$

where, $\rho^n$ $\mathbf{v}^n$, $P^n$, $\varphi^n$ are the known effective mixture density, velocity, pressure and PF variable at time $t^n$ and $\Delta t$ is the positive timestep duration. The effective mixture density is obtained by

$$\rho^n = \rho_1\left(\frac{1+\varphi^n}{2}\right) + \rho_2\left(\frac{1-\varphi^n}{2}\right), \tag{21}$$

The same goes for any other material property that differs between fluids. The guessed values are represented by the superscript $n$, while the superscripts *, **, and *** represent the first, second and third intermediate values of the current timestep iteration, respectively. The solution of the Eq. (20) yields $\mathbf{v}^*$, the first intermediate velocity of iteration $t^{n+1} = t^n + \Delta t$. This intermediate velocity never satisfies the continuity Eq. (1).

**First momentum corrector step:** The momentum Eq. (2) can be written explicitly as

$$\frac{\rho^*\mathbf{v}^{**} - \rho^n\mathbf{v}^n}{\Delta t} + \nabla\cdot(\rho^n\mathbf{v}^n\mathbf{v}^*) = -\nabla P^* + \mu\nabla^2\mathbf{v}^* - \lambda\left(\nabla^2\varphi^n\nabla\varphi^n + \frac{1}{2}\nabla(\nabla\varphi^n\cdot\nabla\varphi^n)\right) - \rho^n\mathbf{g} \tag{22}$$

The rearranging of the Eq. (22) gives the 1st corrected velocity of the iteration as

$$\mathbf{v}^{**} = \Delta t\left[-\nabla P^* + \mu^n\nabla^2\mathbf{v}^* - \lambda\left(\nabla^2\varphi^n\nabla\varphi^n + \frac{1}{2}\nabla(\nabla\varphi^n\cdot\nabla\varphi^n)\right) - \rho^n\mathbf{g} - \nabla\cdot(\rho^n\mathbf{v}^n\mathbf{v}^*)\right] + \rho^n\mathbf{v}^n/\rho^* \tag{23}$$

Everything on the RHS of Eq. (23) is known except the new pressure field $P^*$ which is obtained by taking divergence of the Eq. (23) and rearranging as

$$\nabla^2 P^* = \nabla\cdot\left[\mu^n\nabla^2\mathbf{v}^* - \lambda\left(\nabla^2\varphi^n\nabla\varphi^n + \frac{1}{2}\nabla(\nabla\varphi^n\cdot\nabla\varphi^n)\right) - \rho^n\mathbf{g} - \nabla\cdot(\rho^n\mathbf{v}^n\mathbf{v}^*)\right] - \nabla\cdot\left(\frac{\rho^*\mathbf{v}^{**}}{\Delta t}\right) + \nabla\cdot\left(\frac{\rho^n\mathbf{v}^n}{\Delta t}\right) \tag{24}$$

For the first momentum corrector, the unknown $\nabla\cdot(\rho^*\mathbf{v}^{**})$ becomes zero, since from the continuity equation

$$\nabla\cdot(\rho^*\mathbf{v}^{**}) = -\left(\frac{\rho^* - \rho^n}{\Delta t}\right), \tag{25}$$

we know that $\rho^*$ and $\rho^n$ are the same until $\varphi$ is not updated in the iteration. Hence, the Eq. (24) changes to

$$\nabla^2 P^* = \nabla\cdot\left[\mu^n\nabla^2\mathbf{v}^* - \lambda\left(\nabla^2\varphi^n\nabla\varphi^n + \frac{1}{2}\nabla(\nabla\varphi^n\cdot\nabla\varphi^n)\right) - \rho^n\mathbf{g} - \nabla\cdot(\rho^n\mathbf{v}^n\mathbf{v}^*)\right] + \nabla\cdot\left(\frac{\rho^n\mathbf{v}^n}{\Delta t}\right), \tag{26}$$

for the inner points. For the pressure field on the boundary points, the equation

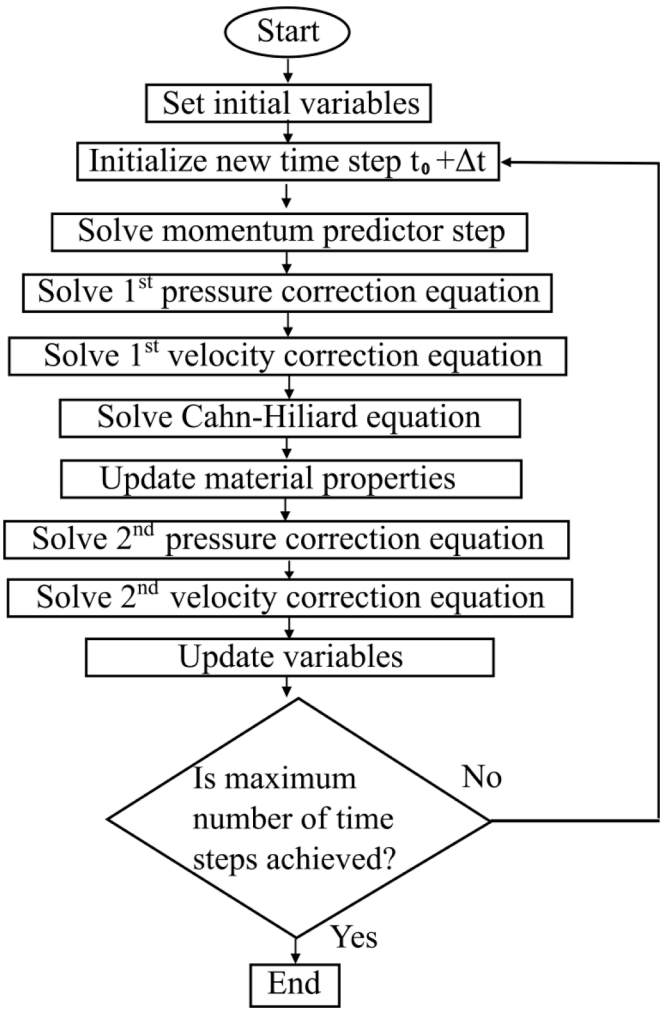


**Fig. 13.** PISO algorithm for two-phase incompressible flow.

$$\mathbf{n}\cdot\nabla P^{*} = \mathbf{n}\cdot\left[\mu^{n}\nabla^{2}\mathbf{v}^{*} - \lambda\left(\nabla^{2}\varphi^{n}\nabla\varphi^{n} + \frac{1}{2}\nabla(\nabla\varphi^{n}\cdot\nabla\varphi^{n})\right) - \rho^{n}\mathbf{g} - \nabla\cdot(\rho^{n}\mathbf{v}^{n}\mathbf{v}^{*})\right] - \mathbf{n}\cdot\left(\frac{\rho^{*}\mathbf{v}^{**}}{\Delta t}\right) + \mathbf{n}\cdot\left(\frac{\rho^{n}\mathbf{v}^{n}}{\Delta t}\right), \tag{27}$$

is used and $\mathbf{v}^{**}$ is the same as the boundary condition of velocity. The solution of the Eq. (26) and (27) gives the first intermediate pressure field $P^{*}$ of the iteration $t^{n+1}$, which is then substituted in the Eq. (23) to get the second intermediate velocity of the iteration $t^{n+1}$.

**PF variable corrector step:** Based on second intermediate velocity obtained from Eq. (23) the PF variable can be updated by solving the Eq. (3) implicitly as

$$\frac{\varphi^{*} - \varphi^{n}}{\Delta t} + \mathbf{v}^{**}\cdot\nabla\varphi^{*} = E\nabla^{2}\psi^{n}, \tag{28}$$

where $\varphi^{n}$ and $\psi^{n}$ are guessed values of PF variables and chemical potential. Rearranging Eq. (28) gives

$$[1 + \Delta t(\mathbf{v}^{**}\cdot\nabla)]\varphi^{*} = \Delta t\left(E\nabla^{2}\psi^{n}\right) + \varphi^{n}. \tag{29}$$

Solution of the Eq. (29) provides updated PF variable.

The material property (density) is updated as

$$\rho^{*} = \rho_{1}\frac{1+\varphi^{*}}{2} + \rho_{2}\frac{1-\varphi^{*}}{2}. \tag{30}$$

**Second momentum corrector step:** For incompressible flows, the 2nd momentum corrector step is just the extension of 1st momentum corrector steps. The equations for the second intermediate pressure field and third intermediate velocity field are as follows

$$\nabla^{2}P^{**} = \nabla\cdot\left[\mu\nabla^{2}\mathbf{v}^{**} - \lambda\left(\nabla^{2}\varphi^{*}\nabla\varphi^{*} + \frac{1}{2}\nabla(\nabla\varphi^{*}\cdot\nabla\varphi^{*})\right) - \rho^{*}\mathbf{g} - \nabla\cdot(\rho^{*}\mathbf{v}^{*}\mathbf{v}^{**})\right] + \nabla\cdot\left(\frac{\rho^{*}\mathbf{v}^{***}}{\Delta t}\right) + \nabla\cdot\left(\frac{\rho^{n}\mathbf{v}^{n}}{\Delta t}\right), \tag{31}$$

$$\mathbf{n}\cdot\nabla P^{**} = \mathbf{n}\cdot\left[\mu\nabla^{2}\mathbf{v}^{*} - \lambda\left(\nabla^{2}\varphi^{*}\nabla\varphi^{*} + \frac{1}{2}\nabla(\nabla\varphi^{*}\cdot\nabla\varphi^{*})\right) - \rho^{*}\mathbf{g} - \nabla\cdot(\rho^{*}\mathbf{v}^{*}\mathbf{v}^{**})\right] - \mathbf{n}\cdot\left(\frac{\rho^{*}\mathbf{v}^{***}}{\Delta t}\right) + \mathbf{n}\cdot\left(\frac{\rho^{n}\mathbf{v}^{n}}{\Delta t}\right), \tag{32}$$

$$\mathbf{v}^{***} = \Delta t\left[-\nabla P^{**} + \mu^{**}\nabla^{2}\mathbf{v}^{**} - \lambda\left(\nabla^{2}\varphi^{*}\nabla\varphi^{*} + \frac{1}{2}\nabla(\nabla\varphi^{*}\cdot\nabla\varphi^{*})\right) - \rho^{*}\mathbf{g}\right] - \nabla\cdot(\rho^{*}\mathbf{v}^{*}\mathbf{v}^{**})\Delta t + \rho^{n}\mathbf{v}^{n}/\rho^{**}, \tag{33}$$

where the unknown $\nabla\cdot(\rho^{*}\mathbf{v}^{***})$ in Eq. (31) can be found through continuity equation as

$$\nabla\cdot(\rho^{*}\mathbf{v}^{***}) = -\left(\frac{\rho^{*} - \rho^{n}}{\Delta t}\right). \tag{34}$$

$P^{**}$, $\rho^{*}$, $\varphi^{*}$ and $\mathbf{v}^{***}$ represent the field values of the time level $t^{n+1}$. These values serve as the initial values of the next time step from $t^{n+1}$ to $t^{n+2}$.

Consistent with the preliminary study [54], the authors also used the two momentum correctors in this work. Generally, the number of momentum correctors can be any whole number greater than or equal to 2, and the number of PF variable corrector steps is always one less than the number of momentum corrector steps. The workflow of the PISO framework for solving PF-formulated two-phase incompressible flow problems is presented in Fig. 13.

### 3.4. Numerical implementation

**For DAM simulations:** The simulations of the present paper use a code based on a previously established meshless library written in modern object-oriented FORTRAN and compiled in Intel Fortran Compiler Version 19.1.1. The numerical code is parallelized using OpenMP, and six threads are used for each computation. The time step size $\Delta t$ of all simulations is restricted by the Courant-Friedrichs Lewy (CFL) and Von Neumann stability conditions as

$$\Delta t = \min\left(\frac{h}{|\mathbf{v}|}, 0.25\frac{h^{2}}{D}\right) \tag{35}$$

where, $h$ is the node spacing measured as the minimum distance between two consecutive nodes and the diffusivity constant. The Courant number [73] of the simulations is Co $= (|v|\Delta t)/h = 0.25$. The simulations are performed until the time $t = \Delta t \times$ No.oftimesteps reaches 0.9s. The input DAM parameters of each simulation are described in their respective discussion in Section 4, but they all align with the preliminary single-phase flow study [54]. The numerical method is verified by comparing the obtained solutions with the reference FVM-VOF solutions at different times.

**For reference FVM-VOF simulations:** The reference numerical simulation in the Cartesian coordinate system is performed with open-source code Gerris [67,68]. For multiphase flow simulation, Gerris uses second-order time and space discretisation, VOF and Piecewise

**Table 3**
Comparison of the computational details of all the node arrangements used in the present work.

| Domain | 2D Cavity | | | | Axisymmetric cavity | | | |
|---|---|---|---|---|---|---|---|---|
| | Uniform node arrangement | | | Non-uniform | Uniform Node arrangement | | | Non-uniform |
| | Coarse $C_{2D}$ | Medium$M_{2D}$ | Fine $F_{2D}$ | $NU_{2D}$ | Coarse $C_{AX}$ | Medium $M_{AX}$ | Fine $F_{AX}$ | $NU_{AX}$ |
| Number of total nodes | 90, 000 | 150, 000 | 210, 000 | 90, 625 | 65, 000 | 105, 000 | 155, 000 | 63, 447 |
| Minimum node spacing $h$[m] | 0.00361 | 0.00284 | 0.00237 | 0.00285 | 0.00348 | 0.00292 | 0.00212 | 0.00298 |
| Time step size [s] | 0.0001 | 0.00002 | 0.00002 | 0.00002 | 0.0001 | 0.00002 | 0.00002 | 0.00002 |
| Time [s] per iteration | 1.34 | 1.89 | 2.68 | 1.40 | 1.25 | 1.67 | 2.34 | 1.36 |
| No. of iterations to reach $t_f = 0.9$s | 9000 | 45,000 | 45,000 | 45,000 | 9000 | 45,000 | 45,000 | 45,000 |
| Computational time [s] to reach $t_f = 0.9$s | 12,060 | 85,050 | 120,600 | 63,000 | 11,250 | 75,150 | 105,300 | 61,200 |

Linear Interface Construction (PLIC) algorithm [74] for interface reconstruction and generalised height function [75] to calculate the local curvature of the interface. The classical CFL condition controls the time step size, and an adaptive mesh refinement algorithm based on the octree division of cells is used, which refines the cells dynamically as the interface grows. The input parameters, initial and boundary conditions are the same as in DAM simulations.

For the validation of axisymmetric DAM-PF simulations, FVM-VOF based OpenFOAM simulations are calculated. The issue of interface smearing in VOF based OpenFOAM simulations is handled by an interface compression approach [76]. An axisymmetric wedge-shaped domain (based on OpenFOAM® requirement) is discretised with uniformly distributed 20,000 non-overlapping hexahedron cells with sizes of 0.01m. The boundary and initial conditions are set such that they replicate DAM-PF problem setup. In FVM-VOF based simulations a second-order vanLeer Total Variation Diminishing (TVD) scheme [77] is used for convective terms. A second-order TVD scheme limitedLinearV [78] is used for interpolation of the velocity field. For temporal integration first-order implicit Euler method is used. The pressure-velocity coupling was handled with PISO algorithm. Adaptive time stepping is utilised with a condition that Courant number stays below 0.25. For further detailed implementation and utilisation the readers are directed to [78].

## 4. Results and discussion

This section is divided into three subsections, explaining the outcomes of the present work. First, a node density independence test is conducted for both geometries to demonstrate the node density convergence. Next, a sensitivity study of DAM parameters is performed to determine suitable input parameters. In the last section, the evolution of the interface position is presented for 2D and axisymmetric cavities at different intervals of flowtime.

### 4.1. Space discretization

The node density independence test is done by testing three uniform and one non-uniform node arrangements for each geometry. The uniform node arrangements are coarse, medium or fine based on their total number of nodes while the non-uniform node arrangement is denser in the region of interest and coarser otherwise. The coarse, medium and fine node arrangements of the 2D cavity are named $C_{2D}$, $M_{2D}$ and $F_{2D}$, respectively, while its non-uniform node arrangement is $NU_{2D}$. Similarly, $C_{AX}$, $M_{AX}$, $F_{AX}$ are the coarse, medium and fine node arrangements of the axisymmetric cavity and $NU_{AX}$ represents its non-uniform node arrangement. The procedure of generating uniform and non-uniform node arrangements is described in the Section 3.2, and the data about their total number of nodes and computational costs is included in Table 3. The non-uniform node arrangements are created in a way that the node density in the region of interest matches with the medium node arrangement, hence the minimum distance between two consecutive nodes $h$ is almost the same for $M_{2D}$ and $NU_{2D}$ for 2D cavity and $M_{AX}$ and $NU_{AX}$ for the axisymmetric cavity. The node density in the coarser areas of each non-uniform node arrangement is six times less than its denser area. This subsection aims to find out if the non-uniform node arrangements provide accuracy similar to that of the finer uniform node arrangement with less computational expense. For this subsection, the shape parameter $a_0$ and the number of nodes in a local subdomain $n_{loc}$ are set to 10.0 and 13, respectively.

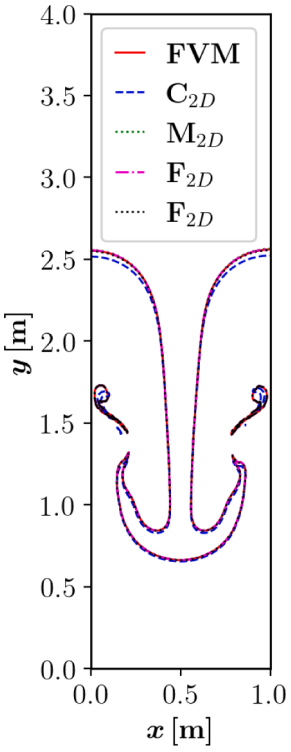


**Fig. 14.** Contours of DAM and FVM with four different node arrangements in 2D cavity at $t = 0.9$s.

The solution of the simulations for all four node arrangements of the 2D and AX cavities and their comparison with the reference FVM-VOF results at $t = 0.9$sare presented in Fig. 14 and Fig. 16, respectively. The comparison is done for the vertical coordinate of the interface position i.e. $y$-coordinate for the 2D domain and $z$-coordinate for the AX domain. A slight difference in the shapes of the interface for coarser node arrangements ($C_{2D}$ for 2D and $C_{AX}$ for AX domain) is observed, while the results for the denser node arrangements ($M_{2D}$ and $F_{2D}$ for the 2D and $M_{AX}$ and $F_{AX}$ for the axisymmetric domain) overlap with their respective reference FVM results which means that the solution for the uniform medium node arrangements $M_{2D}$ and $M_{AX}$ are node density converged with negligible relative errors.

The interface positions for DAM and FVM solutions are extracted from Paraview at 2000 points and their relative error is calculated as $\Delta\varepsilon = (\varepsilon_{DAM} - \varepsilon_{FVM})/\varepsilon_{FVM}$, where $\varepsilon_{DAM}$ and $\varepsilon_{FVM}$ denote the values of the

**Table 4**
Maximum relative error of DAM and FVM solutions for the interface positions of the tested node arrangements.

| Node arrangement | Maximum relative error for the vertical component of the interface position | Node arrangement | Maximum relative error for the vertical component of the interface position |
|---|---|---|---|
| $C_{2D}$ | $2.19 \times 10^{-4}$ | $C_{AX}$ | $2.76 \times 10^{-4}$ |
| $M_{2D}$ | $1.72 \times 10^{-4}$ | $M_{AX}$ | $1.49 \times 10^{-4}$ |
| $F_{2D}$ | $1.55 \times 10^{-4}$ | $F_{AX}$ | $1.36 \times 10^{-4}$ |
| $NU_{2D}$ | $1.68 \times 10^{-4}$ | $NU_{AX}$ | $1.59 \times 10^{-4}$ |

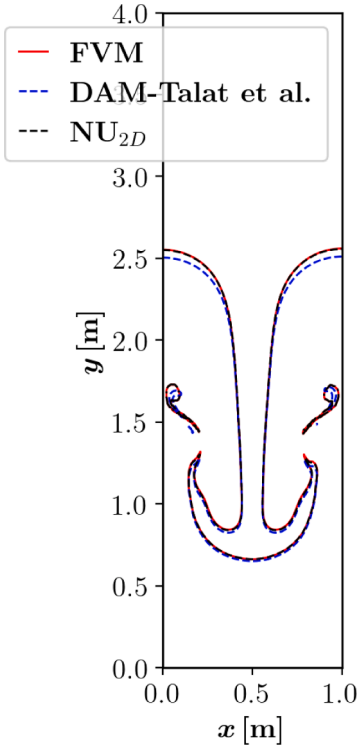


**Fig. 15.** Comparison of contours of present model with the previous meshless model [11] and FVM in 2D cavity at $t = 0.9$s.

vertical coordinate of the interface position obtained using DAM and FVM, respectively. The maximum relative error of each node arrangement is presented in Table 4. It can be seen that the relative error is reduced when a larger number of nodes in uniform node arrangements are used. A larger number of nodes better captures the local variations, such as change in interface position, reducing the approximation error inherent in the numerical method. In the local subdomains, the field values are estimated based on their neighbouring nodes. The distance between the neighbours decreases with the number of nodes, leading to more accurate interpolation and less interpolation error. The reduced interpolation and approximation errors contribute to lower relative error between DAM and reference FVM solutions. It is evident from Table 4 that the accuracy of the solution is achieved at the expense of higher computational cost when constant node density is used all over the domain. On the contrary, the solutions with non-uniform node arrangements exhibit comparable accuracy with considerable reduction in the computational time. The computational time for $NU_{2D}$ is $\sim$ 45% less than $M_{2D}$ for 2D simulations while for AX simulations $\sim$ 37% reduced computational time was observed with $NU_{AX}$ that $M_{AX}$. Therefore, the rest of the 2D simulations are performed with node arrangement $NU_{2D}$ and node arrangement $NU_{AX}$ is used for AX simulations. For 2D simulations, the results for the chosen node arrangement $NU_{2D}$ are afterwards compared with the DAM simulations presented in the study [11] in

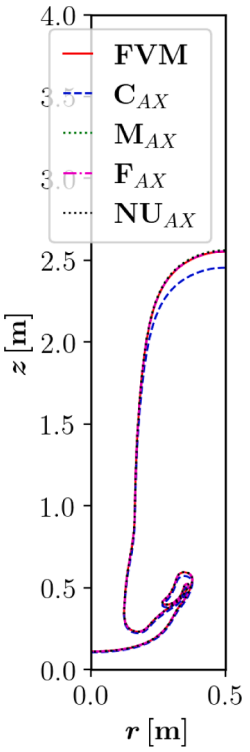


**Fig. 16.** Contours of DAM and FVM with four different node arrangements in axisymmetric cavity at $t = 0.9$s.

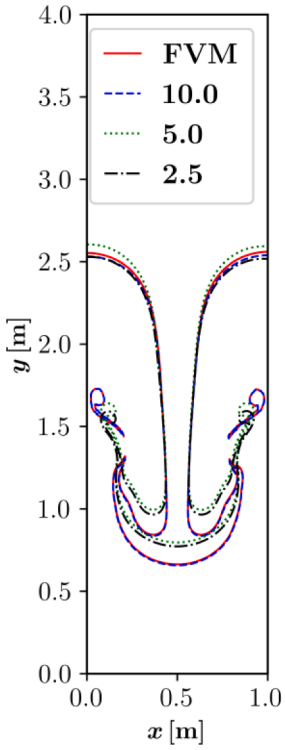


**Fig. 17.** Contours of FVM and DAM solutions for three different shape parameter values for 2D RT cavity.

Fig. 15. Compared to the existing literature, the present model fits better with the Gerris reference results. Notably, the present model possesses an inherent stability of incorporating the density variation throughout the momentum equation, a feature that proved elusive in the

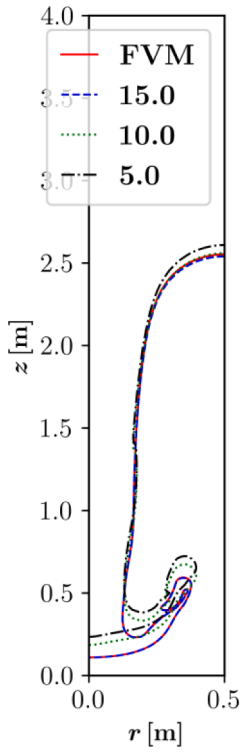


**Fig. 18.** Contours of FVM and DAM solutions for three different shape parameter values for AX RT cavity.

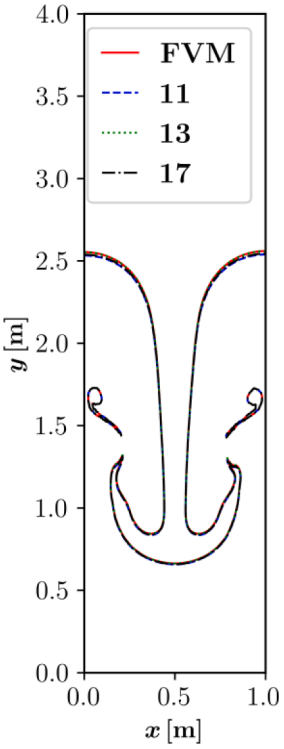


**Fig. 19.** Contours of FVM and DAM solutions for three different number of nodes in a local subdomain for 2D RT cavity at $t = 0.9$s.

study [11]. The capability of this present model to tackle the large density variation (Atwood number of 0.76) gave us the confidence to use the solver for our main application i.e., gas-focused microjets where the density ratio of the fluids is $\sim 6000$.

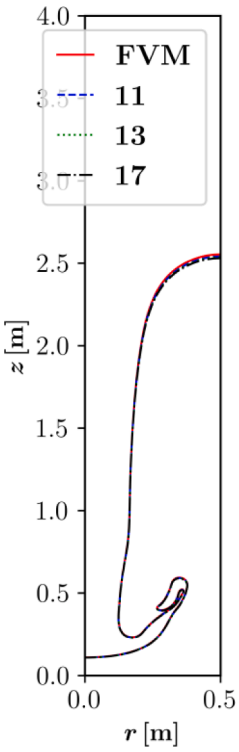


**Fig. 20.** Contours of FVM and DAM solutions for three different number of nodes in a local subdomain for axisymmetric RT cavity at $t = 0.9$s.

### 4.2. Sensitivity study of DAM parameters

To highlight the impact of selecting appropriate input parameters, the sensitivity study of DAM parameters is performed in this subsection. The tested DAM parameters include the shape parameter of the Gaussian weight function $a_0$ and the number of nodes in one local subdomain $n_{loc}$. Initially, three different values of shape parameter $a_0 = 2.5$, 5.0 and 10.0 are investigated for the discussed geometries with 13 nodes in a local subdomain. The results in Fig. 17 and Fig. 18 demonstrate that the lower shape parameters 2.5 and 5.0 fail to capture the correct dynamics of the moving interface for both 2D and axisymmetric coordinates systems.

For 2D cavity, lower shape parameters lead to incomplete detachment of the tails or spikes of the heavier fluid. Conversely, the higher shape parameter facilitates the faster penetration of the heavier fluid into the lighter fluid, resulting in significantly visible bending curves for right and left spikes. The value of shape parameter 10.0 is recommended for similar simulations as it gives better accuracy, and the shape of the interface overlaps with the reference FVM results. The shape parameter decides how gradual the decay of the Gaussian weight function would be from 1 to 0. For higher shape parameters, the central node of the subdomain is the most important one and the rest of the nodes are given less importance which in the present simulations ends with more accurate results. However, the attempts to use the shape parameters larger than 10.0 were unsuccessful, and the solutions diverged quickly. Subsequently, the simulations were performed with three different numbers of the nodes in a local subdomain $n_{loc} = 11$, 13and 17. The results of the

**Table 5**
The computational time of different number of nodes in a local subdomain are compared.

| $a_0$ | $n_{loc}$ | No. of iterations | Time [s] per iteration | Total time [s] |
|---|---|---|---|---|
| 10.0 | 11 | 9000 | 1.33 | 11,970 |
| | 13 | 9000 | 1.40 | 12,600 |
| | 17 | 11,250 | 3.38 | 38,025 |

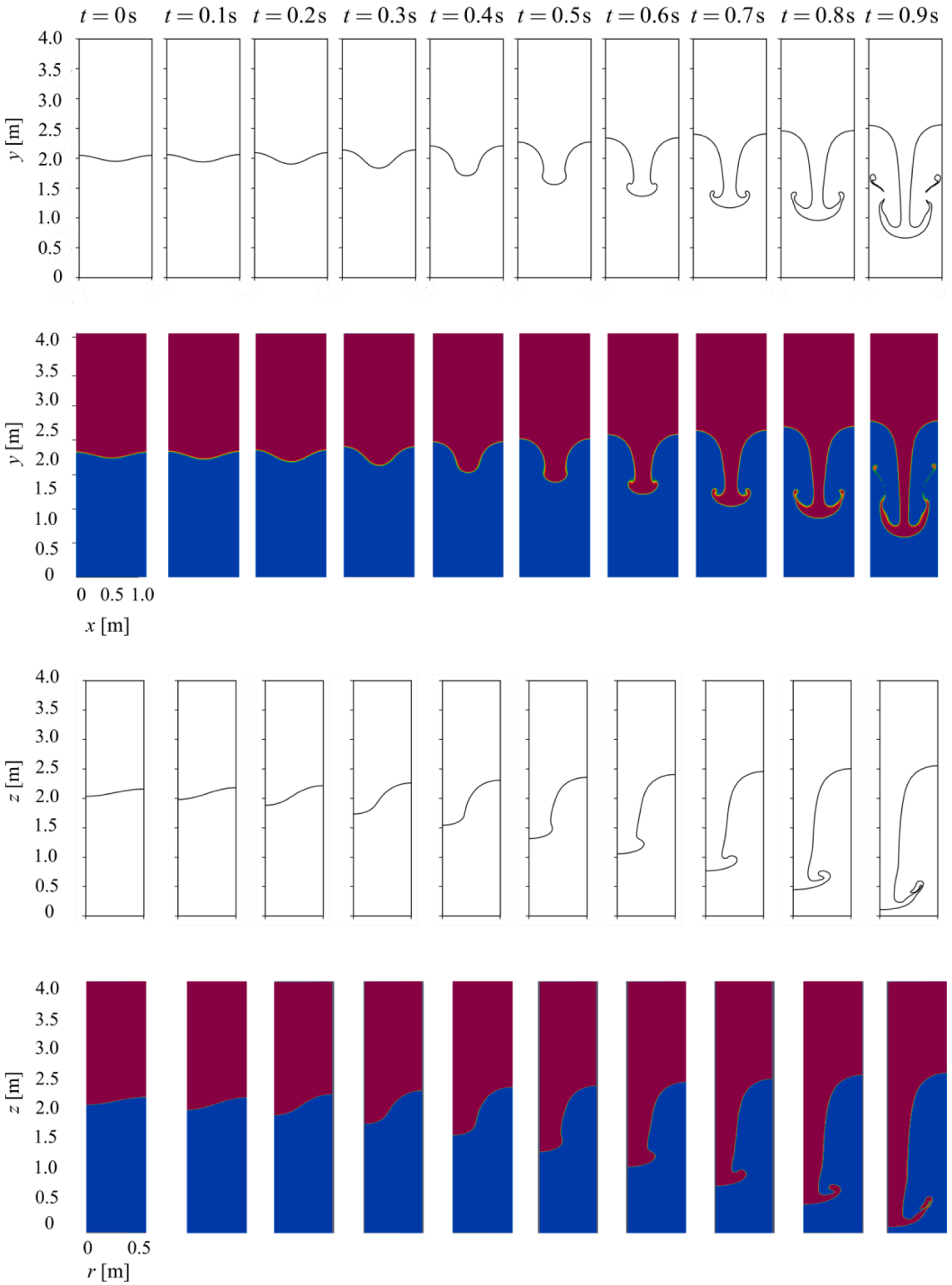


**Fig. 21.** Contours of the time evolution of the interface of the RT instability between two fluids for the 2D cavity (row 1) and for the AX cavity (row 3), Maps of the time evolution of the PF variable for the 2D cavity (row 2) and for the AX cavity (row 4).

interface position for all three values of $n_{loc}$ are presented in Fig. 19 and Fig. 20. They show a negligible variation from the reference FVM solution. No significant differences in the shape of the interface were observed for all three values of $n_{loc}$ in 2D and AX simulations. The effect of $n_{loc}$ on the computational time of the solution is presented in Table 5. The time step size for two smaller values of $n_{loc}$ is $1 \times 10^{-4}$ while for higher value the time step size is $1 \times 10^{-5}$. The increased number of nodes in a local subdomain increases the time required to perform one iteration, which results in higher computational time overall. The solutions with smaller number of nodes in a local subdomain in Fig. 19 and Fig. 20 overlap very well with the reference results and reduce the computational time by~ 30%. Therefore, based on all these findings, the most suitable combination of parameters for the present work shape parameter $a_0 = 10.0$ and $n_{loc} = 13$.

The analysis of the method presented in the previous and present subsections proves that the error between the obtained DAM solutions and the reference FVM solutions can be minimized by using proper node discretisation and suitable input parameters. The next subsection explores how the interface between two fluids changes their shape over time in both discussed geometries.

### 4.3. Time evolution of RT instability

A classical Rayleigh-Taylor instability benchmark test case described in Section 2 is numerically solved in Cartesian coordinates and then extended to axisymmetric coordinates for the first time. The time evolution of the interface at different times is presented in Fig. 21.

The onset of RT instability is triggered by an initial perturbation at $t = 0$s between two fluids of different densities and the same viscosity. For the present simulations, the perturbation is given by a sinusoidal wave of amplitude $A = 0.05$m given in Eq. (6) and Eq. (7) and presented in Fig. 1 and Fig. 2 for 2D and axisymmetric cavities, respectively. The gravitational force is the driving force in RT instability, which accelerates the downward acceleration of the heavier fluid. This acceleration causes a pressure gradient which opposes the gravitational force. When the pressure gradient is not strong enough to balance the gravitational force, the interface becomes unstable, and the initial small perturbation of the interface starts to grow. The lighter fluid starts to penetrate the heavier fluid as bubbles, while the heavier fluid moves into the lighter fluid as spikes. At the initial stages of the simulation, these bubbles and spikes are tiny and move slowly. As the instability grows, they become larger and move quicker.

The surface tension force plays a stabilising role and reduces the growth rate of the instability. Its strong damping effect resists the development of short wavelength disturbances at the interface. At the later stages of RT instability $t > 0.5$s, the surface tension force narrows the RT bubble and accelerates its growth by squeezing. However, the squeezing of the bubble neck appears different for 2D and AX simulations in Fig. 21 because the surface tension force behaves differently in different coordinate systems.

## 5. Conclusions

A novel two-phase, meshless numerical model for two-phase incompressible flow has been developed. The incorporation of PFM in our previously developed DAM and PISO based single-phase flow solver enhanced its capabilities to two-phase flow simulations. The model is equally suitable for 2D and AX arrangements as well as uniform and non-uniform node arrangements. The present study performs the first meshless simulation of the classical RT instability problem in axisymmetric coordinates without the Boussinesq approximation. The obtained results are in excellent agreement with the reference FVM-VOF results and previous 2D meshless numerical study. Based on the sensitivity study regarding DAM parameters, the authors recommend $n_{loc} = 13$ and $a_0 = 10.0$ for similar numerical computation. The successful study demonstrates the accuracy and robustness of the two-phase solver and builds our confidence to utilise it for more complex cases. The formulation of the numerical model is suitable for two Newtonian, incompressible fluids. The interface thickness between the phases is geometry and discretization-dependent and may require adjustment in other types of fluid flow problems. In general, the interface thickness should be two times the minimum distance between two nodes. The model will further be extended for two-phase compressible flow problems, including gas-focused micro-jets.

## CRediT authorship contribution statement

**K.B. Rana:** Writing – original draft, Visualization, Validation, Software, Resources, Methodology, Investigation, Formal analysis, Data curation, Conceptualization. **B. Mavrič:** Writing – review & editing, Software, Resources, Methodology, Conceptualization. **R. Zahoor:** Validation. **B. Šarler:** Writing – review & editing, Supervision, Resources, Project administration, Methodology, Funding acquisition, Conceptualization.

## Declaration of competing interest

The authors declare that they have no known competing financial interests or personal relationships that could have appeared to influence the work reported in this paper.

## Data availability

Data will be made available on request.

## Acknowledgement

Funding for this research is provided by the Slovenian Grant and Innovation Agency (ARIS) within the framework of Young Researcher program, program group P2–0162 and projects J2–4477 and Z2–2640. The research is also partially funded by the Centre of Free Electron Laser (CFEL), DESY, Hamburg, under the project: Innovative methods for imaging with the use of X-ray Free Electron Laser (XFEL) and synchrotron sources: simulation of gas-focused micro-jets. The computations were performed by the high-performance computational resources at the Faculty of Mechanical Engineering, University of Ljubljana. The first author sincerely thanks Dr. Tadej Dobravec from the Faculty of Mechanical Engineering, University of Ljubljana, for valuable discussions about non-uniform node generation and phase-field method.

## References

[1] Rayleigh L. Investigation of the character of the equilibrium of an incompressible heavy fluid of variable density. Proceed London Math Soc 1882;14:170–7. https://doi.org/10.1112/plms/s1-14.1.170.
[2] Taylor GI. The instability of liquid surfaces when accelerated in a direction perpendicular to their planes. I. Proceedings of the royal society of London. Series A, Math Phys Sci 1950;201:192–6. https://doi.org/10.1098/rspa.1950.0052.
[3] Lewis DJ. The instability of liquid surfaces when accelerated in a direction perpendicular to their planes. II. Proceedings of the royal society of London. Series A, Math Phys Sci 1950;202:81–96. https://doi.org/10.1098/rspa.1950.0086.
[4] Segre. E, editor. Collected papers. 1: italy (1921 - 1938) univ. editor. Chicago, USA: of Chicago Press; 1971.
[5] Aref H, Tryggvason G. Model of Rayleigh-Taylor instability. Phys Rev Lett 1989;62:749–52. https://doi.org/10.1103/PhysRevLett.62.749.
[6] Birkhoff G. instability and laminar mixing. Taylor. Los Almos national laboratory report LA-1862; 1956.
[7] Harlow FH, Welch JE. Numerical calculation of time-dependent viscous incompressible flow of fluid with free surface. Phys fluids 1965;8:2182–9.
[8] Daly BJ. Numerical study of two fluid Rayleigh-Taylor instability. Phys fluids 1967;10:297–307. https://doi.org/10.1063/1.1762109.
[9] Tryggvason G. Numerical simulations of the Rayleigh-Taylor instability. J Comput Phys 1988;75:253–82. https://doi.org/10.1016/0021-9991(88)90112-X.
[10] Forbes LK. The Rayleigh–Taylor instability for inviscid and viscous fluids. J Eng Math 2009;65:273–90. https://doi.org/10.1007/s10665-009-9288-9.
[11] Talat N, Mavrič B, Hatić V, Bajt S, Šarler B. Phase field simulation of Rayleigh–Taylor instability with a meshless method. Eng Anal Bound Elem 2018;87:78–89. https://doi.org/10.1016/j.enganabound.2017.11.015.
[12] Young YN, Tufo H, Dubey A, Rosner R. On the miscible Rayleigh–Taylor instability: two and three dimensions. J Fluid Mech 2001;447:377–408. https://doi.org/10.1017/S0022112001005870.
[13] Boussinesq J. Théorie analytique de la chaleur: mise en harmonie avec la thermodynamique et avec la théorie mécanique de la lumière. Gauthier-Villars; 1903.
[14] Ryskin G, Leal LG. Numerical solution of free-boundary problems in fluid mechanics. Part 1. The finite-difference technique. J Fluid Mech 1984;148:1–17. https://doi.org/10.1017/S0022112084002214.
[15] Ryskin G, Leal LG. Numerical solution of free-boundary problems in fluid mechanics. Part 2. Buoyancy-driven motion of a gas bubble through a quiescent liquid. J Fluid Mech 1984;148:19–35. https://doi.org/10.1017/S0022112084002226.
[16] Ryskin G, Leal LG. Numerical solution of free-boundary problems in fluid mechanics. Part 3. Bubble deformation in an axisymmetric straining flow. J Fluid Mech 1984;148:37–43. https://doi.org/10.1017/S0022112084002238.

[17] Tuković Ž, Jasak H. A moving mesh finite volume interface tracking method for surface tension dominated interfacial fluid flow. Comput fluids 2012;55:70–84. https://doi.org/10.1016/j.compfluid.2011.11.003.

[18] Hu HH, Patankar NA, Zhu MY. Direct numerical simulations of fluid-solid systems using the arbitrary Lagrangian–Eulerian technique. J Comput Phys 2001;169:427–62.

[19] Ramaswamy S, Leal LG. The deformation of a viscoelastic drop subjected to steady uniaxial extensional flow of a Newtonian fluid. J Nonnewton Fluid Mech 1999;85:127–63.

[20] Khayat RE. Three-dimensional boundary element analysis of drop deformation in confined flow for Newtonian and viscoelastic systems. Internat J Num Methods Fluids 2000;34:241–75.

[21] Toose EM, Geurts BJ, Kuerten JGM. A boundary integral method for two-dimensional (non)-Newtonian drops in slow Viscous flow. J Nonnewton Fluid Mech 1995;60:129–54.

[22] Zhang DF, Stone HA. Drop formation in viscous flows at a vertical capillary tube. Phys fluids 1997;9:2234–42. https://doi.org/10.1063/1.869346.

[23] Wong H, Rumschitzki D, Maldarelli C. Theory and experiment on the low-Reynolds-number expansion and contraction of a bubble pinned at a submerged tube tip. J Fluid Mech 1998;356:93–124. https://doi.org/10.1017/S0022112097007805.

[24] Sussman M, Smith KM, Hussaini MY, Ohta M, Zhi-Wei R. A sharp interface method for incompressible two-phase flows. J Comput Phys 2007;221:469–505. https://doi.org/10.1016/j.jcp.2006.06.020.

[25] Brackbill JU, Kothe DB, Zemach C. A continuum method for modeling surface tension. J Comput Phys 1992;100:335–54.

[26] Kang M, Fedkiw RP, Liu XD. A boundary condition capturing method for multiphase incompressible flow. J Sci Comput 2000;15:323–60. https://doi.org/10.1023/A:1011178417620.

[27] Hirt CW, Nicholas BD. Volume of fluid (VOF) method for the dynamics of free boundaries. J Comput Phys 1981;39:201–25.

[28] Osher S, Sethian JA. Fronts propagating with curvature-dependent speed: algorithms based on Hamilton-Jacobi formulation. J Comput Phys 1988;79:12–49.

[29] Lowengrub J, Truskinovsky L. Quasi-incompressible Cahn-Hilliard fluids and topological transitions. Proceed Royal Soci London 1998;454:2617–54.

[30] Khalili M, Yahyazadeh H, Gorji-Bandpy M, Ganji DD. Application of volume of fluid method for simulation of a droplet impacting a fiber. Propuls Power Res 2016;5:123–33. https://doi.org/10.1016/j.jppr.2016.04.003.

[31] Zahoor R, Bajt S, Šarler B. Influence of gas dynamic virtual nozzle geometry on micro-jet characteristics. Internat J Multiphase Flow 2018;104:152–65. https://doi.org/10.1016/j.ijmultiphaseflow.2018.03.003.

[32] Zahoor R, Belšak G, Bajt S, Šarler B. Simulation of liquid micro-jet in free expanding high-speed co-flowing gas streams. Microfluid Nanofluidics 2018;22:87. https://doi.org/10.1007/s10404-018-2110-0.

[33] Kim J, Lowengrub J. Phase field modeling and simulation of three-phase flows. Interfaces Free Boundar 2005;7:435–66. https://doi.org/10.4171/IFB/132.

[34] Liu C, Shen J. A phase field model for the mixture of two incompressible fluids and its approximation by a Fourier spectral method. Physica D 2003;179:211–28.

[35] Kim J. Phase-field models for multicomponent fluid flows. Commun Comput Phys 2012;12:613–61.

[36] Liu J, Amberg G, Do-Quang M. Diffuse interface method for a compressible binary fluid. Phys Rev E 2016;93:013121.

[37] Qian T, Wang XP, Sheng P. Molecular scale contact line hydrodynamics of immiscible flows. Phys Rev E 2003;68:016306. https://doi.org/10.1103/PhysRevE.68.016306.

[38] Zhao X, Qian T, Wang Q. Thermodynamically consistent phase field models of multi-component compressible fluid flows. Commun Math Sci 2018;18:1441–68.

[39] Liu J, Wang XP. Phase field simulation of drop formation in a coflowing fluid. Internat J Numer Analy Modell 2015;12:268–85.

[40] Ozisik MN. Finite difference methods in heat transfer. CRC Press; 2017.

[41] Zienkiewicz OC, Taylor RL, Zhu JZ. The finite element method: its basis and fundamentals. Burlington, Canada: Elsevier/Butterworth-Heinemann; 2005.

[42] Versteeg HK, Malalasekera W. An introduction to computational fluid dynamics. The finite volume method. Longman Scient Techn 2007.

[43] Škerget L L, Hriberšek M, Kuhn G. Computational fluid dynamics by boundary-domain integral method. Internat J Numer Methods Eng 1999;46:1291–311. https://doi.org/10.1002/(SICI)1097-0207(19991120)46:8<1291::AID-NME755>3.0.CO;2-O.

[44] Gingold RA, Monaghan JJ. Smoothed particle hydrodynamics: theory and application to non-spherical stars. Mon Not R Astron Soc 1977;181:375–89.

[45] Belytschko T, Lu YY, Gu L. Element-free Galerkin methods. Internat J Numer Methods Eng 1994;37:229–56. https://doi.org/10.1002/nme.1620370205.

[46] Šarler B, Vertnik R. Meshfree explicit local radial basis function collocation method for diffusion problems. Comput Math Applicat 2006;51:1269–82.

[47] Atluri SN, Shen S. The meshless local Petrov- Galerkin (MLPG) method: a simple & less-costly alternative to the finite element and boundary element methods. Comput Modell Eng Sci 2002;3:11–51.

[48] Šarler B, Atluri SN. Recent studies in meshless & other novel computational methods. Duluth, USA: Tech Science Press; 2010.

[49] Vuga G, Mavrič B B, Šarler B. An improved local radial basis function method for solving small-strain elasto-plasticity. Comput Methods Appl Mech Eng 2024;418:116501. https://doi.org/10.1016/j.cma.2023.116501.

[50] Nayroles B, Touzat G, Villon P. Generalizing the finite element method: diffuse approximation and diffuse elements. Comput Mech 1992;10:307–18.

[51] Hatić V, Mavrič B, Košnik N, Šarler B. Simulation of direct chill casting under the influence of a low-frequency electromagnetic field. Appl Math Model 2018;54:170–88. https://doi.org/10.1016/j.apm.2017.09.034.

[52] Rana KB, Zahoor R, Mavrič B, Šarler B. Development and verification of meshless diffuse approximate method for simulation of compressible flow between parallel plates. J Phys Conference Ser 2021;2116:012021. https://doi.org/10.1088/1742-6596/2116/1/012021.

[53] Rana KB, Zahoor R, Mavric B, Šarler B. Development and verification of meshless diffuse approximate method for simulation of single phase, compressible flow in axisymmetry. In: Proceedings of CHT-21 ICHMT international symposium on advances in computational heat transfer Rio de Janeiro; 2021. p. 411–23. https://doi.org/10.1615/ICHMT.2021.CHT-21.330.

[54] Rana KB, Mavrič B, Zahoor R, Šarler B. A meshless solution of the compressible viscous flow in axisymmetric tubes with varying cross-sections. Eng Anal Bound Elem 2022;143:340–52. https://doi.org/10.1016/j.enganabound.2022.06.029.

[55] Oñate E, Idelsohn S. A mesh-free finite point method for advective-diffusive transport and fluid flow problems. Comput Mech 1998;21:283–92. https://doi.org/10.1007/s004660050304.

[56] Oñate E, Idelsohn S, Zienkiewicz OC, Taylor RL. A finite point method in computational mechanics. Applications to convective transport and fluid flow. Internat J Numer Methods Eng 1996;39:3839–66. https://doi.org/10.1002/(SICI)1097-0207(19961130)39:22<3839::AID-NME27>3.0.CO;2-R.

[57] Oñate E, Idelsohn S, Zienkiewicz OC, Taylor RL, Sacco C. A stabilized finite point method for analysis of fluid mechanics problems. Comput Methods Appl Mech Eng 1996;139:315–46. https://doi.org/10.1016/S0045-7825(96)01088-2.

[58] Prax C, Sadat H, Salagnac P. Diffuse approximation method for solving natural convection in porous media. Transp Porous Media 1996;22:215–23. https://doi.org/10.1007/BF01143516.

[59] Prax C, Sadat H, Dabboura E. Evaluation of high order versions of the diffuse approximate meshless method. Appl Math Comput 2007;186:1040–53. https://doi.org/10.1016/j.amc.2006.08.059.

[60] Wang CA, Sadat H, Prax C. A new meshless approach for three-dimensional fluid flow and related three-dimensional problems. Comput fluids 2012;69:136–46. https://doi.org/10.1016/j.compfluid.2012.08.017.

[61] Sadat H, Prax C. Application of the diffuse approximation for solving fluid flow and heat transfer problems. Int J Heat Mass Transf 1996;39:214–8. https://doi.org/10.1016/S0017-9310(96)85018-6.

[62] Šarler B, Vertnik R, Perko J. Application of diffuse approximate method in convective-diffusive solidification problems. Comput, Mater Continua 2005;2:77–83.

[63] Hatić V, Rek Z, Mramor K, Mavrič B, Šarler B. A meshless solution of a of lid-driven cavity containing a heterogeneous porous medium. Mater Sci Eng 2020;861:012028. https://doi.org/10.1088/1757-899X/861/1/012028.

[64] Hatič V, Mavrič B, Šarler B. Simulation of a macrosegregation benchmark with a meshless diffuse approximate method. Internat J Numer Methods Heat Fluid Flow 2018;28:361–80. https://doi.org/10.1108/HFF-04-2017-0143.

[65] Hatič V, Mavrič B, Šarler B. Meshless simulation of a lid-driven cavity problem with a non-Newtonian fluid. Eng Anal Bound Elem 2021;131:86–99. https://doi.org/10.1016/j.enganabound.2021.06.015.

[66] Talat N, Mavrič B, Belšak G, Hatić V, Bajt S, Šarler B. Development of meshless phase field method for two-phase flow. Internat J Multiphase Flow 2018;108:169–80. https://doi.org/10.1016/j.ijmultiphaseflow.2018.06.003.

[67] Popinet S. Gerris: a tree-based adaptive solver for the incompressible Euler equations in complex geometries. J Comput Phys 2003;190:572–600. https://doi.org/10.1016/S0021-9991(03)00298-5.

[68] Popinet S. An accurate adaptive solver for surface-tension-driven interfacial flows. J Comput Phys 2009;228:5838–66. https://doi.org/10.1016/j.jcp.2009.04.042.

[69] C.J. Greenshields. OpenFOAM user Guide 2022.

[70] Issa RI. Solution of the implicitly discretised fluid flow equations by operator-splitting. J Comput Phys 1986;62:40–65. https://doi.org/10.1016/0021-9991(86)90099-9.

[71] Chorin AJ. A numerical method for solving incompressible viscous flow problems. J Comput Phys 1997;135:118–25. https://doi.org/10.1006/jcph.1997.5716.

[72] Finkel RA, Bentley JL. Quad trees a data structure for retrieval on composite keys. Acta Informatica 1974;4:1–9. https://doi.org/10.1007/BF00288933.

[73] Courant R, Friedrichs K, Lewy H. On the partial difference equations of mathematical physics. IBM J Res Dev 1967;11.

[74] Sato Y, Ookawara S, Ogawa K. Visualization and VOF modeling of large bubble rising in narrow fixed bed. J Chem Eng Japan 2010;43:17–22. https://doi.org/10.1252/jcej.09we070.

[75] Cummins SJ, Francois MM, Kothe DB. Estimating curvature from volume fractions. Comput Struct 2005;83:425–34. https://doi.org/10.1016/j.compstruc.2004.08.017.

[76] Weller HG. A new approach to VOF-based interface capturing methods for incompressible and compressible flow. Techn. Report 2008;13.

[77] vanLeer B. Towards the ultimate conservative difference scheme. V. A second-order sequel to Godunov's method. J Comput Phys 1979;32:101–36.

[78] Moukalled F, Mangani L, Darwish M. The finite volume method in computational fluid dynamics. an advanced introduction with openfoam and matlab. London, USA: Springer; 2016.